AD-A277 175

|||||||||||||||||||||||||||||

242100-3-F
Final Report

NEAR-FIELD SHIP WAKE SIGNATURE MODELING AND
SIMULATION

D. LYZENGA
N. MALINAS

Center for Earth Sciences
Advanced Concepts Division

DTIC
ELECTE
MAR 17 1994
S B D

January 1994

94-08590

|||||||||||||||||||||||||||||

94 3 16 117

DISCLAIMER NOTICE
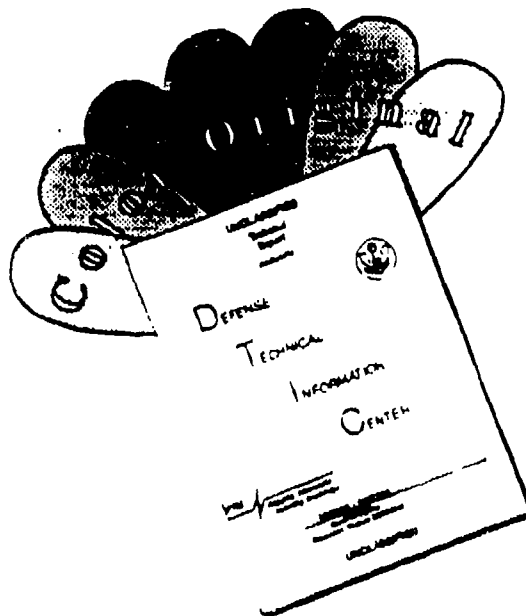
THIS DOCUMENT IS BEST QUALITY AVAILABLE. THE COPY FURNISHED TO DTIC CONTAINED A SIGNIFICANT NUMBER OF COLOR PAGES WHICH DO NOT REPRODUCE LEGIBLY ON BLACK AND WHITE MICROFICHE.

REPORT DOCUMENTATION PAGE

Public reporting burden for this collection of information is estimated to average 1 hour per response, including the time for reviewing instructions, searching existing data sources, gathering and maintaining the data needed, and completing and reviewing the collection of information. Send comments regarding this burden estimate or any other aspect of this collection of information, including suggestions for reducing this burden, to Washington Headquarters Services, Directorate for Information Operations and Reports, 1215 Jefferson Davis Highway, Suite 1204, Arlington, VA 22202-4302, and to the Office of Management and Budget, Paperwork Reduction Project (0704-0188), Washington, DC 20503.

1. AGENCY USE ONLY (Leave blank)	2. REPORT DATE January 1994	3. REPORT TYPE AND DATES COVERED Final 3/92 - 12/93

4. TITLE AND SUBTITLE Near-Field Ship Wake Signature Modeling and Simulation	5. FUNDING NUMBERS N00014-91-C-0266

6. AUTHOR(S)

D. Lyzenga
N. Malinas

7. PERFORMING ORGANIZATION NAME(S) AND ADDRESS(ES) Environmental Research Institute of Michigan (ERIM) P.O. Box 134001 Ann Arbor, MI 48113-4001	8. PERFORMING ORGANIZATION REPORT NUMBER 242100-3-F

9. SPONSORING/MONITORING AGENCY NAME(S) AND ADDRESS(ES) Office of Naval Research 800 N. Quincy Street Arlington, VA 22217-5000	10. SPONSORING/MONITORING AGENCY REPORT NUMBER

11. SUPPLEMENTARY NOTES

12a. DISTRIBUTION/AVAILABILITY STATEMENT Unlimited	12b. DISTRIBUTION CODE

13. ABSTRACT (Maximum 200 words)

A frequently observed characteristic of Synthetic Aperture Radar (SAR) imagery of moving ships is an area of increased backscatter immediately behind the ship extending approximately one ship length. The region causing these signatures has been termed the near-field disturbed water (NFDW) region of the ship. In this report a simple prediction model for these signatures is presented. This model utilizes a Fourier transform solution for the Kelvin wake along with a numerical procedure for calculating the hull pressure distribution. The model appears to predict the breaking regions more or less correctly for ship hulls having a rectangular stern, but over predicts the extent of the breaking regions for non-rectangular stern shapes. This limitation is apparently due to the fact that energy dissipation due to wave breaking has not been included. Outputs from the NFDW model are used to simulate a SAR image of the NFDW region and encouraging agreement between the appearance of the simulated and actual SAR images is found. The dependence of the NFDW with ship speed is in agreement with observations.

14. SUBJECT TERMS			15. NUMBER OF PAGES 40
			16. PRICE CODE

17. SECURITY CLASSIFICATION OF REPORT Unclassified	18. SECURITY CLASSIFICATION OF THIS PAGE Unclassified	19. SECURITY CLASSIFICATION OF ABSTRACT Unclassified	20. LIMITATION OF ABSTRACT Unlimited

NSN 7540-01-280-5500

⑨ ERIM

CONTENTS

FIGURES

1.0 INTRODUCTION

A frequently observed characteristic of Synthetic Aperture Radar (SAR) imagery of moving ships is an area of increased backscatter immediately behind the ship and extending for approximately one ship length. The region causing these signatures has been termed the near-field disturbed water (NFDW) region of the ship. As part of the Wakes program we have characterized the SAR signatures of this region under a variety of ship and environmental conditions (Malinas, 1992), and have begun a modeling effort with the goal of being able to predict the appearance of these NFDW returns. The model we have developed is based on a Fourier transform solution of the linearized boundary conditions with an applied pressure field. A procedure was developed for calculating the pressure field for a given hull shape and ship speed, and this pressure field was used for calculating the near-field Kelvin wake. A wave breaking criterion was then applied to the vertical acceleration computed from this model in order to estimate the extent of the breaking regions. The fluid velocities within the breaking regions were computed, and the radar cross section was assumed to be proportional to the breaking area. The radar cross section and fluid velocity were used to generate a simulated SAR image which can then compared with an actual SAR image. A description of the data set used in this analysis is given in Section 2. In Section 3 a model for the NFDW returns is presented and the model predictions are analyzed and compared with SAR measurements in Section 4. Finally, in Section 5 conclusions are made and a recommended course of action is presented.

1

2.0 BACKGROUND

SAR observations of range travelling ships are useful for investigating the NFDW signature because the ship is displaced from the wake thus allowing an analysis of the wake feature without significant interference from the ship return. These images are also interesting because an azimuthal displacement of the *wake* itself has been observed, indicating that relatively large Doppler shifts or scatterer velocities occur within the NFDW. For the work described in this report, one particular data set of this type was chosen and additional parametric variations were considered.

SAR data were collected by the ERIM/NAWC P-3 during the 1989 ONR Ship Wake Experiment (Lyden, 1989) under a range of operating and imaging conditions. The SAR imagery for FFG Run 7-2 (Figure 1) was collected with the ship traveling in the range direction at 17 knots and at a relatively large incidence angle (65 degrees). In this data the ship is displaced in azimuth due to the doppler shift associated with the ship's velocity. Bright returns are located in range near the bow and stern of the ship extending in azimuth from the actual ship position toward the displaced ship position. Thus, these returns appear to have doppler shifts ranging from nearly zero up to a maximum value which is near the ship speed. Furthermore, the features are slightly tilted, indicating that the doppler shift appears to decrease with distance aft. Measurements of the apparent wake velocity are presented in (Malinas, 1992) for this particular case and other range traveling cases as well. These measurements correspond to the maximum observed velocities of the wake feature for each range cell.

Because of the range locations of these bright returns, it seems reasonable to associate them with the breaking bow (or shoulder) and stern waves. Figure 2 contains aerial photos of frigates traveling at two speeds illustrating these breaking waves. The return near the stern is brighter and extends to larger Doppler shifts than

2

FFG Run 7-2 1/31

L-VV

L-HH

X-VV

C-VV

Ground Range (m)

0

1100

0

800

Azimuth (m)
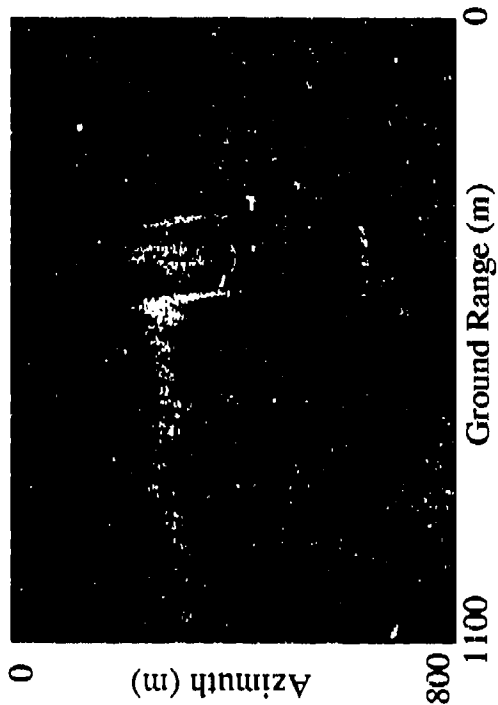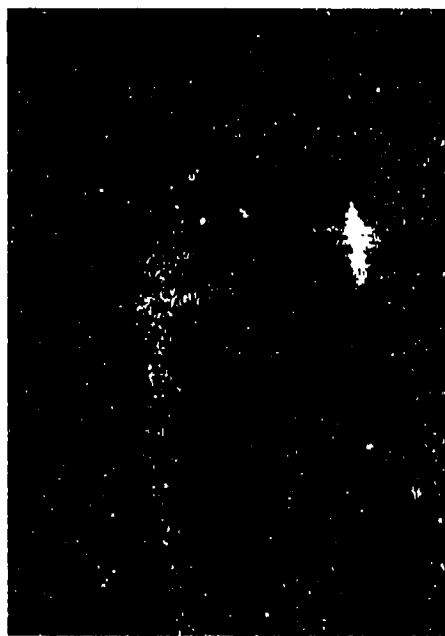
Ship Speed: 17 knots   Incidence Angle: 65 deg.   Wind Speed: 10.2 knots   Rel. Wind. Dir: -84 deg.

Figure 1:   Four Channel Imagery for FFG Run 7-2 1/31 (Range Traveling Ship).

3

Aerial Photograph

FFG - 10 (Keel Dome)

18 knot

463 m

98 m
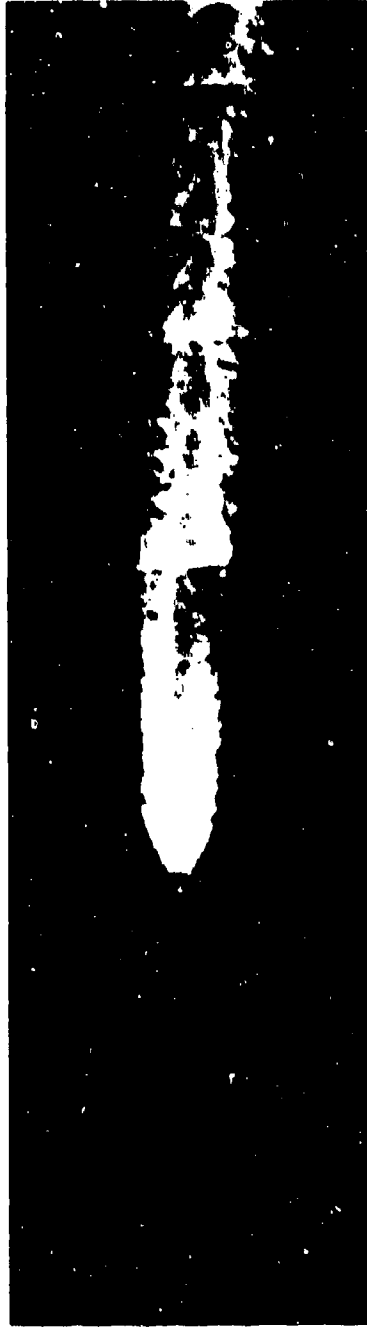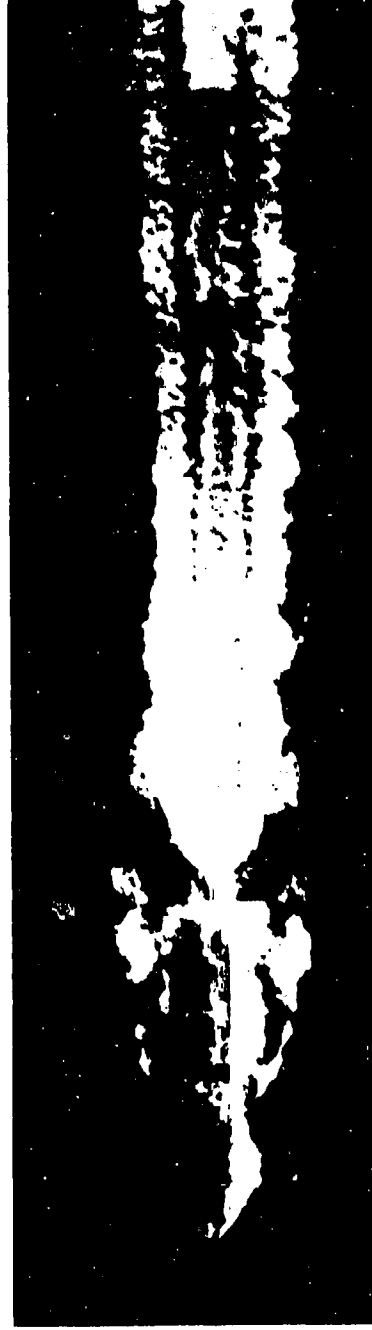
25 knot

453 m

109 m

Figure 2a: Aerial Photograph of FFG-10 (Keel Dome) at 18 and 25 Knots.

4

Aerial Photograph
FF-1067 (Bow Dome)

18 knot

455 m

25 knot

433 m

93 m
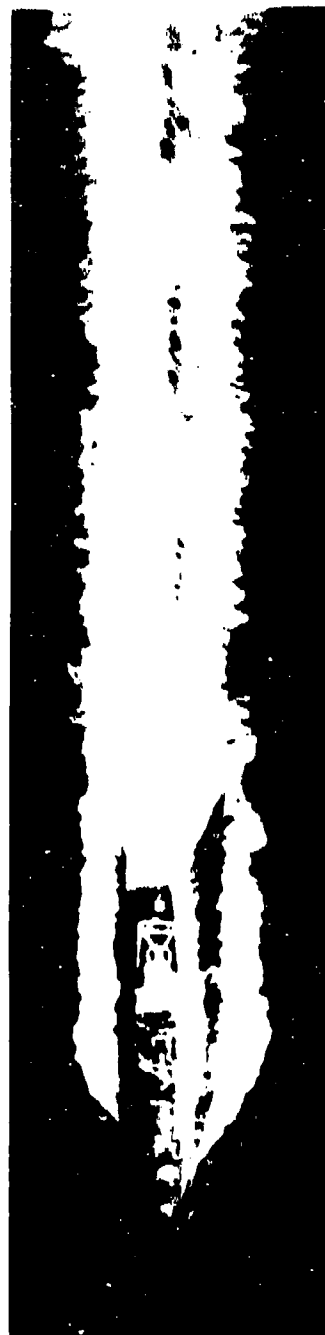
157 m

Figure 2b: Aerial Photograph of FFG-10 (Bow Dome) at 18 and 25 Knots.

5

the return near the bow. We have undertaken a modeling effort in order to try to predict at least some aspects of the observed signature. The region near the ship hull is extremely complex and difficult to model adequately, and we realize that the work presented here represents a simplified and perhaps overly simplistic treatment of the problem. However, we hope that this preliminary study will provide some basis or motivation for additional investigations in this area.

3.0 WAKE MODEL

The model used in this study is based on a Fourier transform solution of the linearized boundary conditions with an applied pressure field

$$p(x,y) = p_o + \rho f(x,y)e^{\epsilon t} \tag{1}$$

in a coordinate system moving with the ship, where the exponential growth term is used as a device to satisfy the radiation condition (Whitham, 1974). The velocity potential is assumed to be of the form

$$\phi = -U_s x - U_s^2 t + \Phi \tag{2}$$

where U_s is the ship speed (in the $+x$ direction) and Φ is the perturbation potential induced by the ship. The linearized boundary conditions are then

$$\eta_t - U_s \eta_x - \Phi_z = 0$$
$$\Phi_t - U_s \Phi_x + g\eta = -f(x,y)e^{\epsilon t} \tag{3}$$

at $z=0$. The velocity potential must also satisfy Laplace's equation, of course. A Fourier transform solution of this set of equations can be written as

$$\eta(x,y,t) = e^{\epsilon t} \int \int A(k_x,k_y)e^{i(k_x x + k_y y)} dk_x dk_y \tag{4}$$

and

$$\Phi(x,y,z,t) = e^{\epsilon t} \int \int B(k_x,k_y)e^{i(k_x x + k_y y) + kz} dk_x dk_y \tag{5}$$

where $k = \sqrt{k_x^2 + k_y^2}$. Substituting these into the boundary conditions yields

$$A(k_x,k_y) = \frac{kF(k_x,k_y)}{(k_x U_s + i\epsilon)^2 - gk} \tag{6}$$

7

and

$$B(k_x,k_y) = \frac{(\epsilon - ik_x U_s)F(k_x,k_y)}{(k_x U_s + i\epsilon)^2 - gk} \tag{7}$$

where $F(k_x,k_y)$ is the Fourier transform of $f(x,y)$.

3.1   NUMERICAL KELVIN WAKE CALCULATIONS

During the first phase of this project, we used a very crude approximation for the pressure distribution, namely, the hydrostatic pressure on a rectangular hull. These results provided encouraging agreement between the modeled locations of the breaking regions and the observations from the aerial photographs. During the second phase we made two improvements. First, we used a better approximation to the hull shape by digitizing an aerial photograph of the ship and applying a taper along and across the hull. Secondly, we implemented a procedure for calculating the applied pressure distribution required to produce a surface displacement corresponding to the assumed hull shape. Figure 3 outlines the algorithm implemented for this modeling activity. The complete end-to end simulation is performed through three programs; *wake1, wake2, and sarwakesim*. This modeling procedure is as follows.

The surface elevation is calculated for a delta-function pressure distribution using the equation

$$h(x,y) = \frac{\Delta x \Delta y}{(2\pi)^2} \int_{-k_{mx}}^{k_{mx}} \int_{-k_{my}}^{k_{my}} \frac{gke^{-ik_x U/\omega_m}}{(k_x U_s + i\epsilon)^2 - gk} e^{i(k_x x + k_y y)} dk_x dk_y \tag{8}$$

where $k_{mx} = \pi/\Delta x$, $k_{my} = \pi/\Delta y$, and Δx and Δy are the grid spacings in the along-track and across-track directions. The phase term involving $\omega_m = \sqrt{gk_{mx}}$ was added to compensate for a shift in the surface elevation pattern which occurs when the wake is

8

CES-94-003-1

SARWAKESIM

Calculate Radial Velocity in Breaking Regions → Apply Doppler Shift with Smearing → SAR Simulation Output

WAKE 2

Calculate Vertical Acceleration at (x,y) → $a_z(x,y)$ → $-a_z(x,y) > g/2$?

No

Yes → Add to Breaking Region Mask → Calculate Reflectivity → RCS

Scatterer Lifetime

=>

WAKE 1

Ship Speed → Calculate Surface Elevation for δ-Pressure Distribution → Calculate Hull Pressure Distribution → Calculate Velocity Potential → φ(x,y)
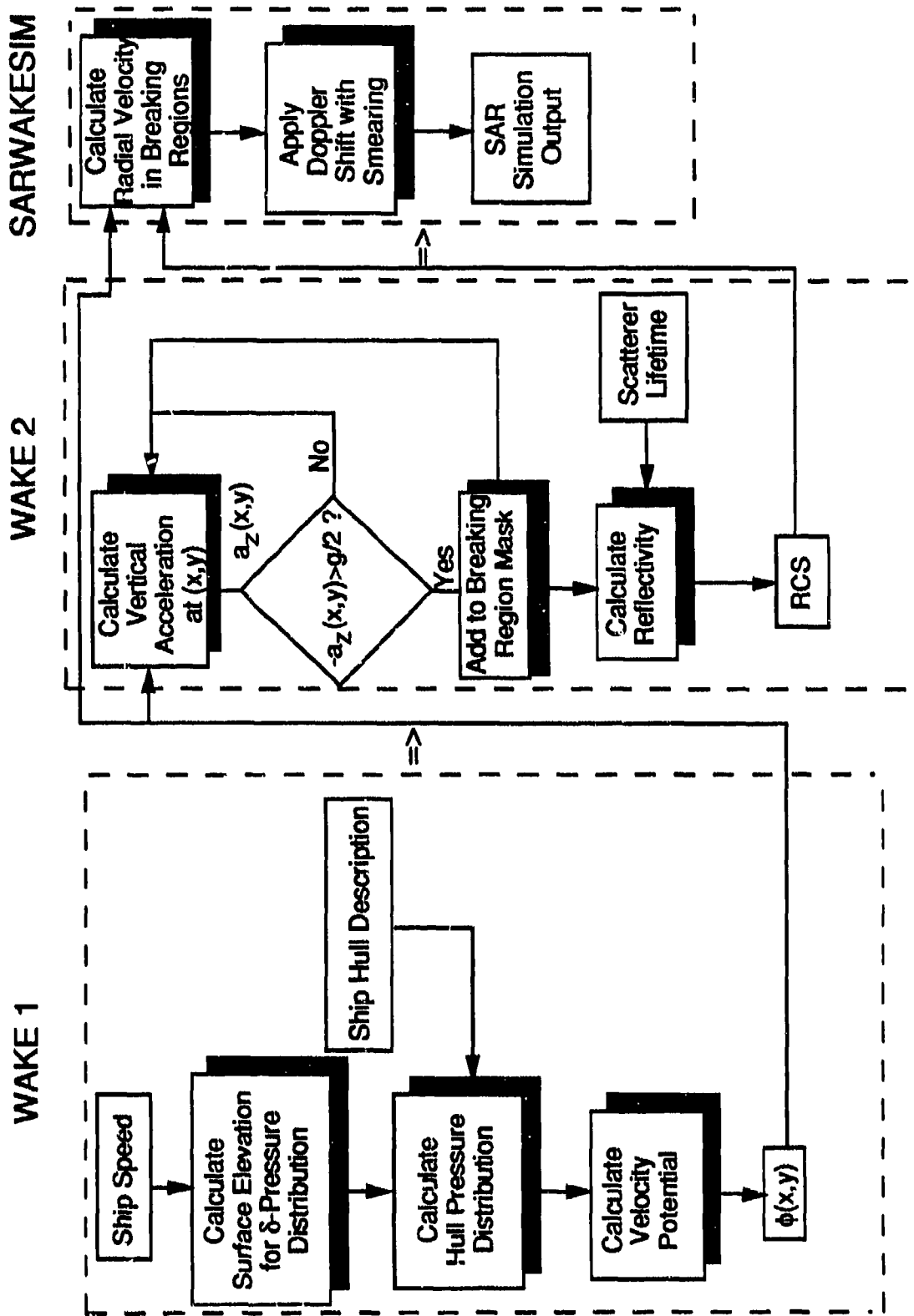
Ship Hull Description

=>

Figure 3: NFDW Model Algorithm Flowchart.

9

computed on a finite grid and with a finite value of ϵ (see below).

The surface elevation is specified at N points on the ship hull and the pressure at these locations is obtained by solving the set of N equations

$$H(x_m,y_m) = \frac{1}{\rho g} \sum_{n=1}^{N} p(x_n,y_n) h(x_m+x_n, y_m+y_n) \qquad (9)$$

for the pressure $p(x_n,y_n)$. This set of linear equations is solved by re-writing Eq.(9) as a matrix equation involving the point source elevation matrix, h, and inverting the equation by multiplying both sides by h^{-1}, i.e.

$$\vec{p} = h^{-1}\vec{H} \qquad (10)$$

where the jth element of $\vec{H}$ and $\vec{p}$ corresponds to the location (x_j,y_j) on the ship hull, and h_{ij} is the surface elevation at the location (x_j,y_j) due to a point source at the location (x_i,y_i). The solution of h^{-1} is calculated using LU decomposition with forward and back substitution (Press et. al., 1986). Note that for $U_s=0$, h becomes a diagonal matrix and $\vec{p}_i$ reduces to the hydrostatic pressure on the hull.

The Fourier transform of the pressure distribution obtained by this procedure was calculated and the result was used to calculate the surface elevation and the velocity potential function outside the hull region, i.e.

$$\eta(x,y) = \frac{1}{\nu} \int\int \frac{k \vec{p}(k_x,k_y)}{(k_x U_s + i\epsilon)^2 - gk} e^{i(k_x x + k_y y)} dk_x dk_y \qquad (11)$$

and

$$\Phi(x,y) = \frac{1}{i\rho} \int\int \frac{(k_x U_s + i\epsilon)\, \hat{p}(k_x,k_y)}{(k_x U_s + i\epsilon)^2 - gk}\, e^{i(k_x x + k_y y)}\, dk_x dk_y \qquad (12)$$

where

$$\hat{p}(k_x,k_y) = \frac{e^{-ik_x U/\omega_m}}{(2\pi)^2} \int\int p(x,y) e^{-i(k_x x + k_y y)}\, dxdy . \qquad (13)$$

The fluid velocity and the apparent vertical acceleration in an earth-fixed coordinate system were then calculated from the velocity potential as

$$v_x = \phi_x + U_s = \Phi_x \quad v_y = \phi_y = \Phi_y \quad v_z = \phi_z = \Phi_z \qquad (14)$$

and

$$a_z = \phi_{zt} - U_s \phi_{zx} = \Phi_{zt} - U_s \Phi_{zx} . \qquad (15)$$

The wake obtained from this procedure depends on the hull shape or pressure distribution, of course, but also on the value of the parameter ϵ. In the analytic theory, this parameter is allowed to approach zero, but in the numerical procedure a finite value must be used in order to avoid wraparound in the FFT domain. From equations (8), (11) and (13), the energy spectrum is equal to the product of the energy spectrum of the impulse response function $h(x,y)$ and the spectrum of the pressure distribution $p(x,y)$. The spectrum of $h(x,y)$ is confined to a small region surrounding the hourglass-shaped curve defined by

$$k_x^2 U_s^2 = gk \qquad (16)$$

which has a minimum wavenumber (where $k_y=0$) given by $k_m = g/U_s^2$. Note that Eq.(16) is for a ship traveling in the x direction. The spectrum of $h(x,y)$ will rotate

11

as the ship direction changes. Figure 4 illustrates the spectral shape of a Kelvin wave and its velocity dependence (again for a ship traveling in the x direction). The spectral energy density along this curve is given by

$$|\tilde{h}_p(k_x,k_y)|^2 = \frac{g^2 k^2}{\epsilon^2(\epsilon^2+4k_x^2 U_s^2)} \approx \frac{gk}{4\,\epsilon^2} \qquad (17)$$

and the 3-dB width of the spectrum in the k_x-direction is approximately

$$\delta k_x = \frac{4\epsilon k^2}{U_s(k_x^2+2k_y^2)} . \qquad (18)$$

The total energy in the spectrum of $h(x,y)$ is then approximately given by the product of the peak spectral density and the spectral width, integrated in the k_y direction. This product turns out to be independent of the ship speed, provided that we choose:

(1) $\delta k_x = 2\Delta k_x = 4\pi/L_x$, in order to have two discrete wavenumber samples within the support region of $\tilde{h}(k_x,k_y)$;

(2) $L_x = 12.8\lambda_m$, where $\lambda_m = 2\pi U_s^2/g$, in order to keep the same number of transverse Kelvin wavelengths within the computational domain;

(3) $k_m = k_{max}/10$ in order to keep the spectrum within the FFT domain, i.e. to have an adequate sample spacing relative to the transverse Kelvin wavelength.

The spectrum of $p(x,y)$ has two components; one corresponding to the hydrostatic pressure or hull shape, which is assumed not to change with ship speed, and the other due to the dynamic pressure which increases roughly as the square of the ship speed. The spectrum of the hydrostatic pressure is expected to have an oscillatory structure (depending on the hull size) superimposed on a roughly k^{-2} to

Kelvin Wake Spectrum
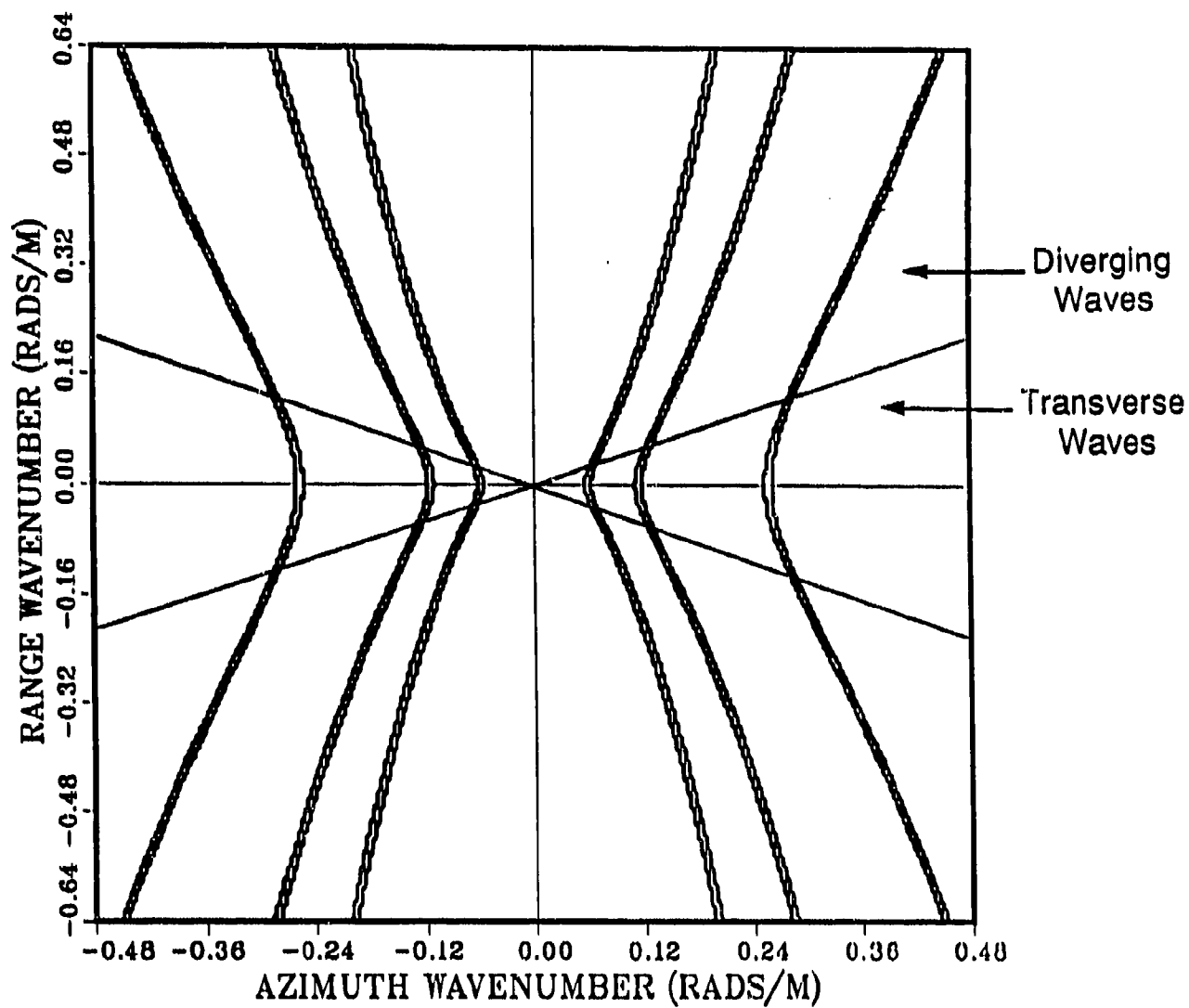## 12, 18, 25 Knots

Figure 4:   Spectral Characteristics of Kelvin Waves for Ship Speeds of 12, 18, and 25 Knots.

k^{-4} falloff (depending on the hull shape). For example, a rectangular hull with dimensions D_x and D_y would produce a hydrostatic pressure spectrum of the form

$$|\beta_s(k_x,k_y)|^2 \propto sinc^2(k_xD_x/2)sinc^2(k_yD_y/2) \tag{19}$$

which falls off like k^{-2}, while a triangular hull with the same dimensions at the waterline would produce a hydrostatic pressure spectrum of the form

$$|\beta_s(k_x,k_y)|^2 \propto sinc^4(k_xD_x/4)sinc^4(k_yD_y/4) \tag{20}$$

which falls off like k^{-4}. Since the wavenumber location of the support region for $\tilde{h}(k_x,k_y)$ scales as g/U_s^2, the wavenumber falloff of the hydrostatic component implies that the wake energy generated by this component is proportional to U_s^4 for the rectangular hull and U_s^8 for the triangular hull. The wave drag D_w, which is given by the total wake energy divided by the length of the computational domain, is then proportional to U_s^2 and U_s^6 for these two cases, and the normalized wave resistance coefficient

$$C_w = \frac{D_w}{\rho U_s^2 L^2} \tag{21}$$

is independent of ship speed for the rectangular hull and proportional to U_s^4 for the triangular hull. The dynamic pressure, on the other hand, is nearly a delta-function in the spatial domain and thus its wavenumber spectrum is nearly flat. Since the magnitude of this pressure spike is proportional to U_s^2, its spectrum and the wave

14

energy produced by this component are both proportional to U_s^4, implying that the wave resistance coefficient is independent of ship speed for this component.

3.2 BREAKING WAVE PREDICTIONS

The next stage in the modeling effort was to use the Kelvin wake model described above to predict regions in the near field region where wave breaking is expected to occur. This is a somewhat controversial subject, and is open to the fundamental criticism that it is inconsistent to use linear wave theory to attempt to predict the highly nonlinear phenomenon of wave breaking (this point is addressed by Longuet-Higgins, 1969). Nonetheless, encouraging results have been presented by several investigators suggesting that the approach may have merit despite these conceptual difficulties.

It is well known that water waves have a limited range of amplitudes, beyond which the wave "breaks" and the motion becomes chaotic in the region of the breaking wave crest. Exact solutions of the wave equations exist for the steady-state case, which show that the wave crest becomes sharper as the wave approaches its limiting amplitude. However, the conditions required for the onset of breaking are not well understood, particularly in the general time-dependent case when a broad spectrum of wavelengths is present. Phillips (1958) suggested that waves break when the vertical acceleration at the crest exceeds the gravitational acceleration g, while Longuet-Higgins (1969) argued for the value $g/2$, which is the maximum downward acceleration at the crest of a Stokes wave. Snyder and Kennedy (1983) used this criterion to predict the occurrence of whitecaps and found reasonable agreement with limited field data.

An empirical wave breaking criterion was determined from a set of laboratory measurements by Ochi and Tsai (1983), and these results were reinterpreted by Srokosz (1986) as being consistent with a limiting downward acceleration of $0.4g$.

15

However, it was pointed out by Longuet-Higgins (1985) that for finite-amplitude waves there is a distinction between the apparent acceleration, as measured by a wave probe at a fixed location, and the real or Lagrangian acceleration experienced by a given parcel of water. In addition, he showed that the apparent vertical acceleration is theoretically unlimited but the real acceleration for steady waves is always less than $0.4g$. However, he also argued that for a superposition of waves with different wavelengths the real downward acceleration could conceivably attain a value of g. Observations by Ewing *et al.* (1987) showed a maximum real downward acceleration of about $0.38g$ and apparent downward accelerations as large as $1.6g$, but there was no indication as to whether these waves were breaking.

For our application, the apparent vertical acceleration was computed by noting that in an earth-fixed coordinate system the velocity potential function becomes

$$\Phi'(x,y,z,t) = \Phi(x - U_s t, y, z, t) \tag{22}$$

so that the vertical acceleration in this coordinate system is given by

$$a_z = \Phi'_{zt} = \Phi_{zt} - U_s \Phi_{zx} = \int\int k(\epsilon - ik_x U_s) B(k_x, k_y) e^{k(k_x x + k_y y)} dk_x dk_y. \tag{23}$$

This equation was used to calculate the vertical acceleration at each point in the scene, and a threshold was applied to select the pixel locations where wave breaking is predicted to occur on the basis of this criterion. In the following, unless otherwise noted, a threshold of $g/2$ is used as the breaking criterion.

The effect of breaking is to produce foam and small-scale surface roughness, both of which are assumed to decay exponentially, with different time constants. The reflectivity resulting from the production and exponential decay of foam and/or surface roughness can be modeled as

$$r(i,j) = r_o b(i,j) + \alpha\, r(i+1,j) \qquad (24)$$

where i and j are position indices in the along-track and across-track directions, respectively, r_o is the reflectivity of actively breaking regions, $b(i,j)$ is a breaking index which is equal to 1 if $a_z < -g/2$ and 0 elsewhere, and

$$\alpha = e^{-\beta\Delta x/U_a} \qquad (25)$$

where β is the temporal decay rate of the foam or surface roughness. This expression must be evaluated by stepping through the grid from right to left, i.e. from larger to smaller values of i .

The reflectivity of breaking waves seems to be on the order of 0.5 for electromagnetic radiation with wavelengths shorter than a few centimeters (Lewis and Olin, 1980; Jessup et al, 1991). This has also been confirmed by recent X-band laboratory measurements at the University of Michigan (Walker et al, 1993). Therefore, the same equation was assumed to apply, with possibly different values of β , for both visible and radar backscatter. In the simulations to be described, a value of $\beta = 0.5$ Hz was used.

3.3 SAR SIMULATIONS

SAR images are dependent on both the reflectivity and the motion of the ocean surface. This dependence is described by the SAR impulse response function, which is proportional to the finite-resolution Doppler spectrum of the backscattered signal, i.e. the Doppler spectrum as computed over a time interval equal to the SAR integration time (Hasselmann et al, 1985; Lyzenga, 1986). Thus, a collection of scatterers located at the along-track position x is mapped into a region of the image

17

centered at the along-track position $x' = x + \frac{R}{V}V_r(x)$ and having a width $\delta x = \frac{R}{V}\sigma_v$

where R is the range, V is the platform velocity, $V_r(x)$ is the mean radial velocity or the centroid of the Doppler spectrum for the scatterers at the location x, and σ_v is the standard deviation of these velocities, or the width of the Doppler spectrum.

In order to simulate the SAR image of the near-field disturbed water, the reflectivity and the surface velocity was computed at each grid cell as discussed in the previous sections. The mean radial velocity was computed as

$$V_r = V_x \cos\phi \sin\theta + V_y \sin\phi \sin\theta + V_z \cos\theta \qquad (26)$$

where θ is the incidence angle and ϕ is the SAR look direction, defined such that $\phi=0$ if the ship is moving toward the SAR, i.e. the x-axis points toward the SAR ground track, and $\phi=\pi/2$ if the y-axis points toward the ground track. A nominal value of $\sigma_v=0.5$ m/s was assumed, and the reflectivity was distributed over the SAR image using the mapping procedure described above. For comparison with data collected by the ERIM/NAWC P-3 SAR, the Doppler spectrum was cut off at a frequency of 0.92m^{-1} in order to account for the effect of the presum filter. A more detailed description of the attenuation effects of the presum filter is presented in (Malinas, 1991).

3.4   MODEL PARAMETERS

Runs of the model were performed to observe the parametric dependencies of hull structure and ship speed and for comparison to aerial photos and SAR data. The hull structures used, although more complicated than the rectangular box shape described earlier, are still very simple structures. Detailed hull structures are available for several ship types (Kuhn, 1992 , Hoekstra, 1991), however, the simple

18

hull structures used in this analysis are adequate for observing first order dependencies. The hull structures are defined by three characteristics; (1) the hull shape of the ship at the water line from an overhead view ; (2) the sub-surface along-hull shape and (3) the sub-surface cross-hull shape. The waterline hull shape was obtained by digitizing an aerial photograph of a frigate class ship (Figure 5). Three types of taper were considered for the sub-surface cross-hull; rectangular, triangular, and semi-circular (Figure 6). These tapers extend from bow to stern on the ship. For example, the triangular hull has a constant draft down the middle of the ship from bow to stern, regardless of the cross-track position. The along-hull taper was limited to three possible cases; (1) no taper at all and (2) a slight tapering at the bow and stern of the ship and (3) a taper at the bow only. Modifications to the code for other structures is trivial, however, these simple structures provide a means for observing the effect of hull shape on the amount of wave breaking predicted by the model. Note that *any* hull structure may be input into the model with the single limitation that only one elevation may be specified under the ship hull for each location. Thus, bulbous bows currently cannot be implemented. This limitation results from the algorithm which calculates the pressure distribution and can be avoided by specifying the pressure distribution directly. In the next section an analysis of the results produced by this model is provided.
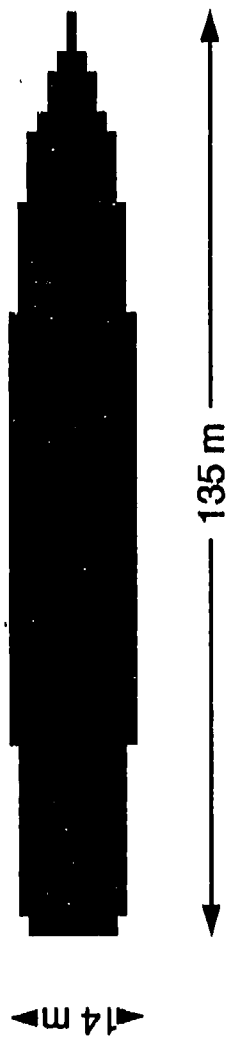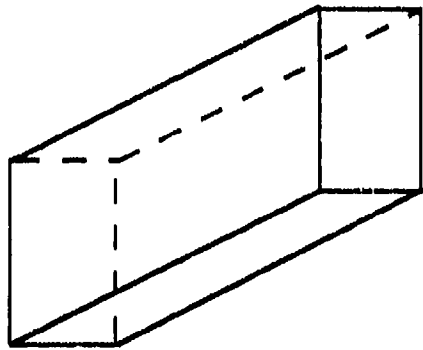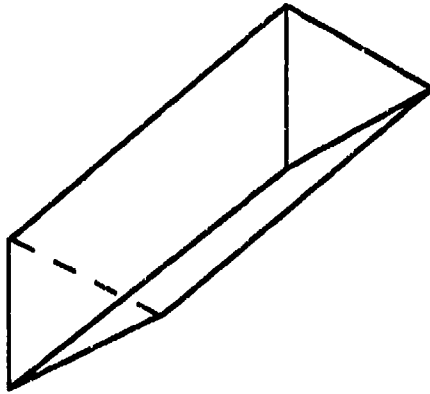
19

Frigate Hull Shape - Top View

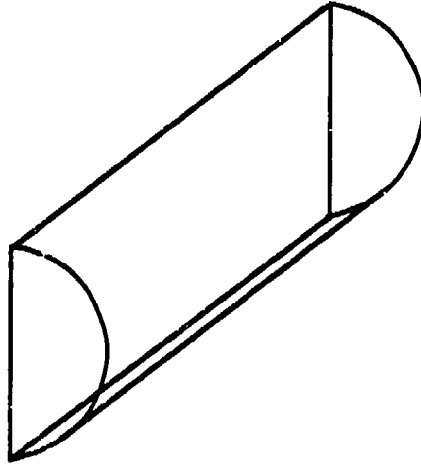**Figure 5:**   Frigate Hull Shape Digitized From Figure 2.

CROSS-HULL SUB-SURFACE TAPER

Rectangle

Triangle

Semi-Circle

ALONG-HULL SUB-SURFACE TAPER

None

Tapered

Figure 6: Sub-surface Tapers Implemented in Model.

4.0 RESULTS AND DISCUSSION

In this section an examination of the model results as a function of speed and hull shape is presented. First an example run illustrating the model outputs will be shown in Section 4.1 and then comparisons between the trends predicted by theory and those observed in actual SAR images will be made in Section 4.2.
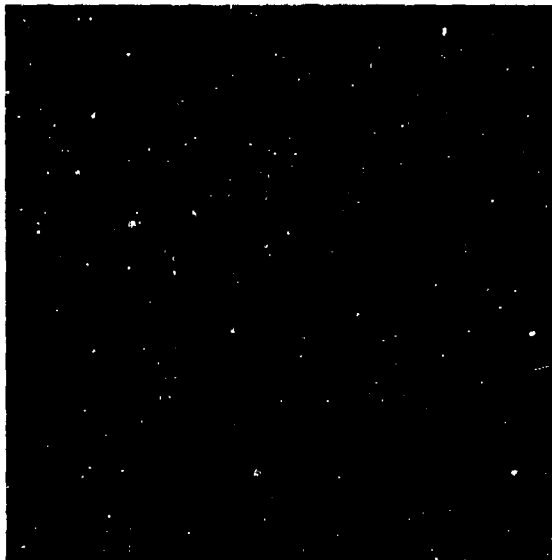
4.1 MODEL OUTPUT EXAMPLE

Figure 7 shows the output of the program *wake1* (refer to Figure 3). The hull shape in this example has a waterline outline of a frigate shape with a constant 5 meter draft at all hull locations. The upper left image shows the surface elevation for a point source moving at 9.5 m/s and in the upper right is the calculated pressure distribution for the same speed. For the most part, the pressure is flat across the hull. There is a notable increase in the pressure, however, at the bow region which appears to correspond to the dynamic pressure discussed in section 3.1. The lower left image is the resulting surface elevation for the ship hull and the lower right shows a scan through the ship center in the along track direction. Within the defined region of the ship, the surface elevation values are equal to the specified ship draft. Modifications to this hull shape will be discussed in Section 4.2. In this example, the sample spacing of the domain was 2.9 m in both the along-track and cross-track directions. Recall from Section 3.1 that the sample spacing in the along-track direction is dependent upon the ship speed, however the cross-track sample spacing is arbitrary.

Figure 8 shows the different output files which are generated by the programs *wake2* and *sarwakesim*. This result is for a frigate water line shape but this time with a triangular sub-surface shape in the cross-hull direction. Again the modeled ship is traveling at 9.5 m/s. The top left is the surface elevation file which is generated by *wake1*. The top right image is the radial velocity which is derived from the velocity potential. The lower left image is a map illustrating the locations of the breaking

22

Calculated Pressure

Surface Elevation Through Ship Center

Point Source Elevation
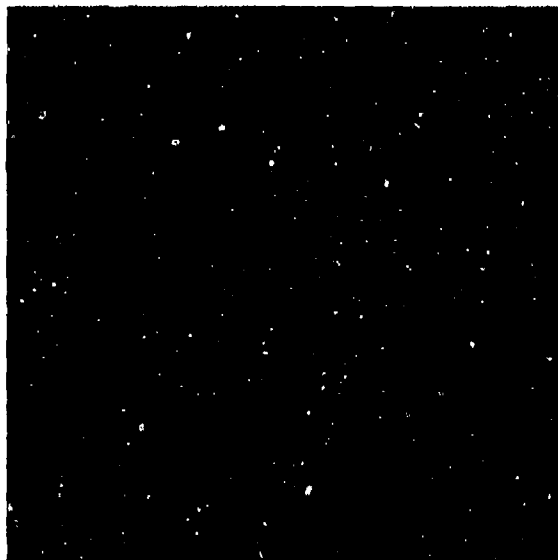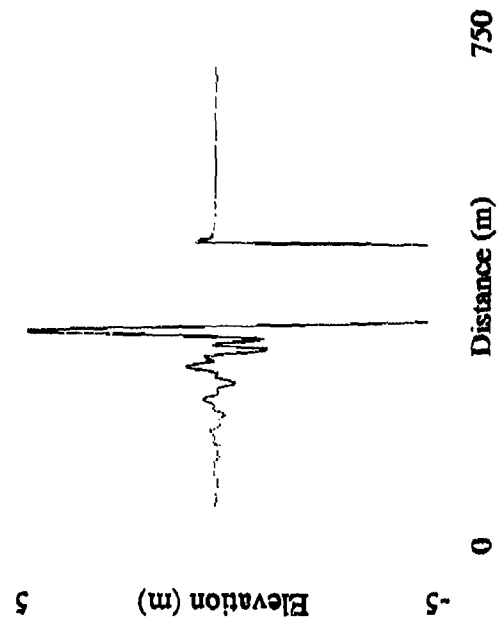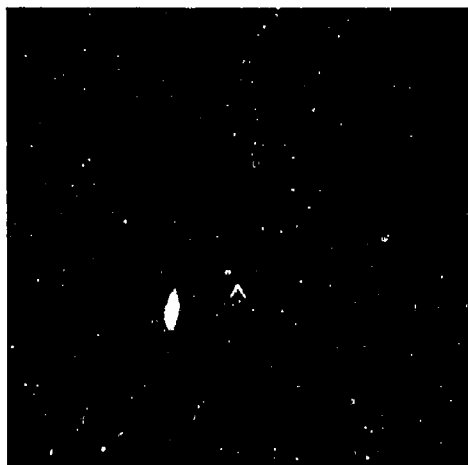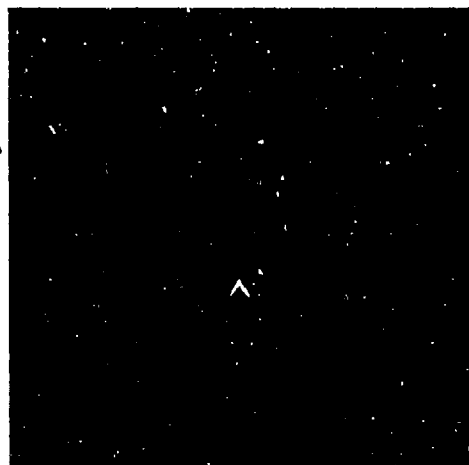
Calculated Surface Elevation

Figure 7:   Example of Program *Wake1* Output.
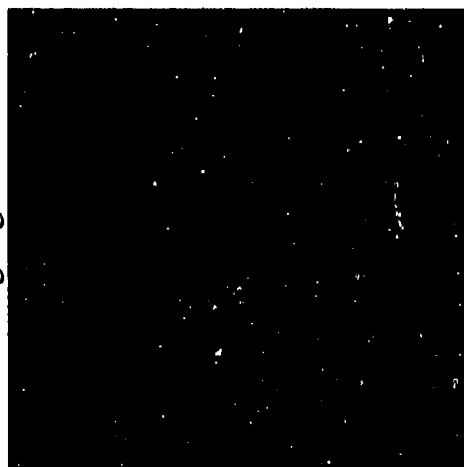
23

Model Output Example
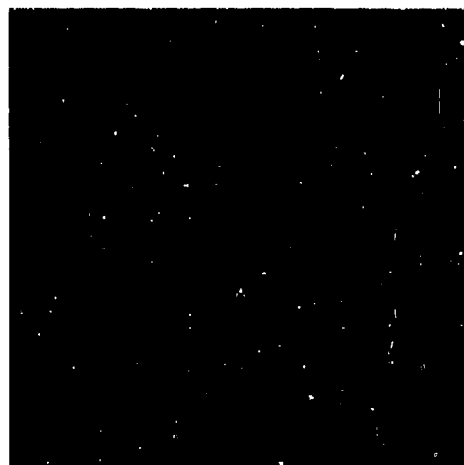
Surface Elevation

Radial Velocity

Breaking Region Mask

Radar Cross Section

SAR Simulation

Figure 8: Example of Program *Wake2* and *Sarwakesim* Output.

24

regions determined by comparison of the vertical acceleration at each point with the acceleration threshold $g/2$. This map can be compared to the aerial photographs in Figure 2 where many similarities exist between the structure of the breaking region and the white foam in the photo. Two particular features stand out; (1) the bow (and shoulder) breaking regions and (2) the stern breaking region which fans out. The bottom center image is the reflectivity which is generated by assuming a radar cross section for a breaking cell and applying an exponential decay. Lastly, the lower right image is the SAR simulation which is generated by applying the SAR impulse response function to the radar cross section. Observe that the ship appears at the bottom of the image, displaced due to its radial motion. If the ship were traveling in the same direction as the SAR platform, much smaller Doppler shifts would result and the wake signature would be concentrated nearer to the ship track. Note that no SAR modeling of the ship return itself is taking place other than shifting its position based upon its radial velocity.

4.2   PARAMETRIC MODEL EXAMPLES

Up to this point, we have provided an overview of the model execution and outputs but have not yet compared the results with theory and SAR observations. In this section we provide a few examples to illustrate the dependence of the breaking regions on hull structure and ship speed and make comparisons to SAR data observations.

Figure 9 shows a comparison of the modeled breaking regions and SAR intensity data for the frigate example shown in Figure 1. Results for both X- and L-bands are shown. The determination of the breaking region is independent of electromagnetic considerations, but a frequency dependence is introduced into *sarwakesim* by the presum filter effect discussed in Section 3.3. Because the Doppler frequency shift due to radial motion is inversely proportional to wavelength, the ship

25

Data/Model Comparison
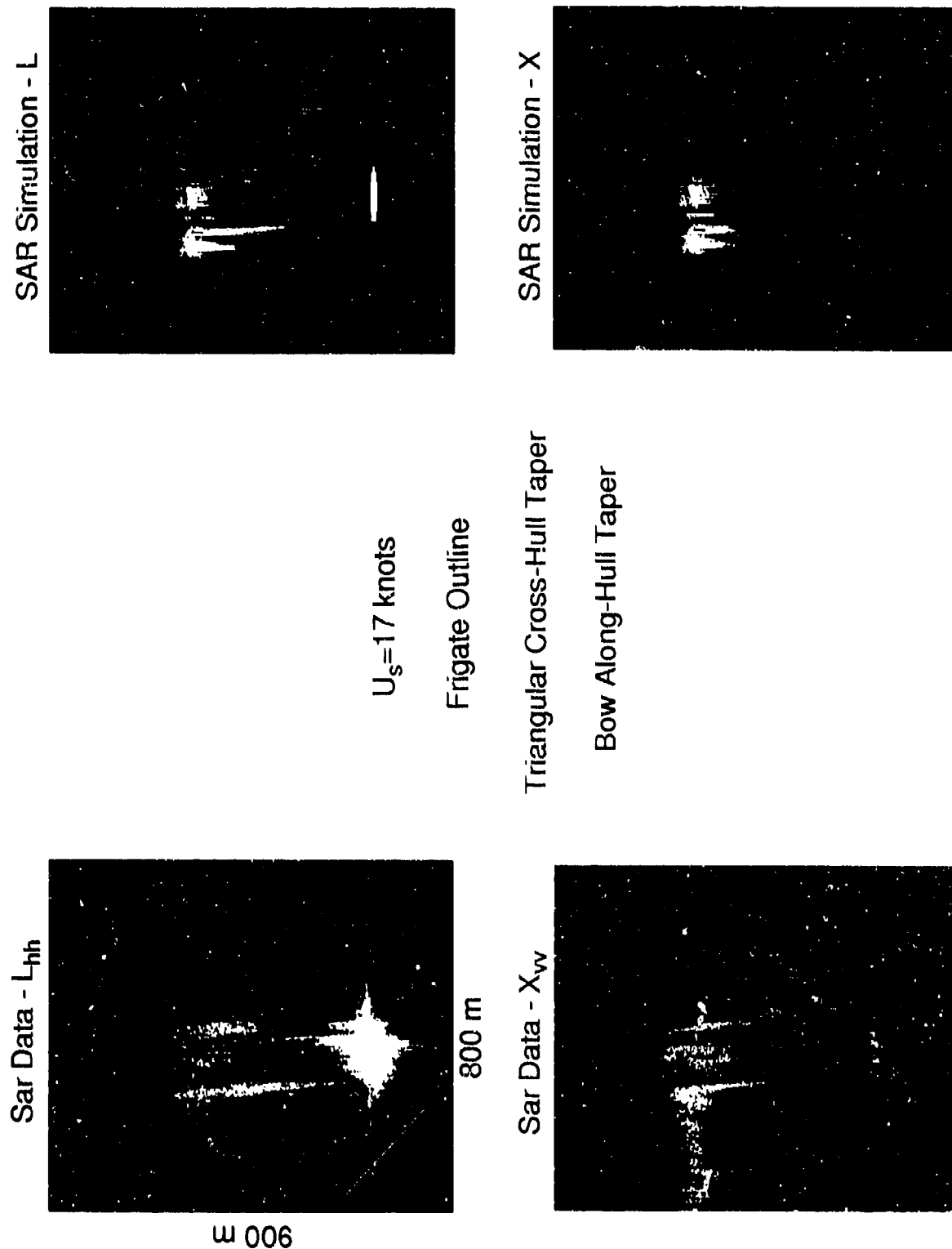

SAR Simulation - L

SAR Simulation - X

Sar Data - L_{hh}

Sar Data - X_{vv}

U_s=17 knots

Frigate Outline

Triangular Cross-Hull Taper

Bow Along-Hull Taper

800 m

900 m

Figure 9: NFDW Model / SAR Data Comparison For FFG Run 7-2.

26

Hull Shape Comparison
Frigate Outline U_s=9.5 m/s

Along-Hull Taper

Cross-Hull Taper

Breaking Region: 702 m^2

Along-Hull Taper

Cross-Hull Taper

Breaking Region: 414 m^2

Along-Hull Taper

Cross-Hull Taper

Breaking Region: 1917 m^2

Along-Hull Taper

Cross-Hull Taper

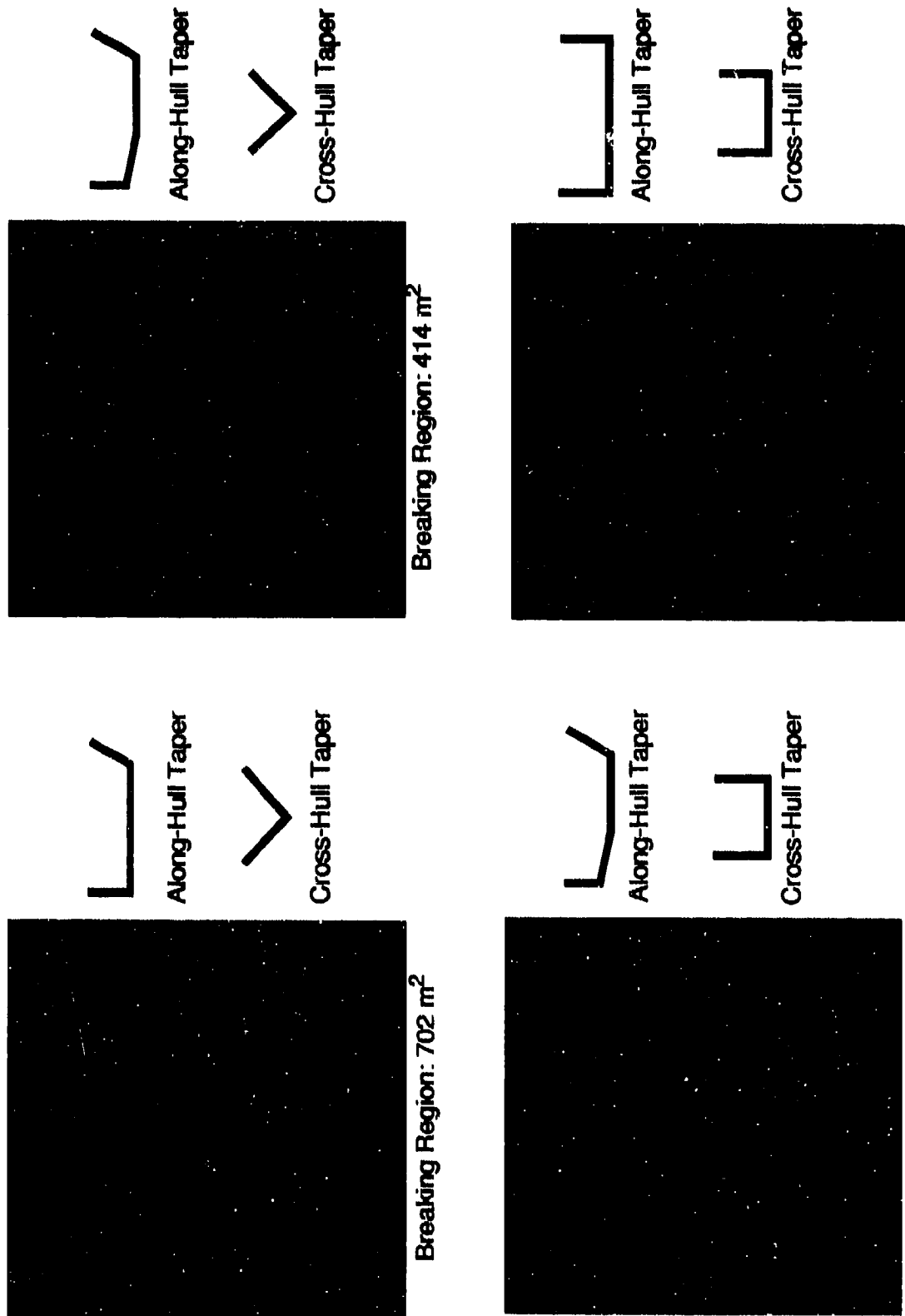Breaking Region: 2205 m^2

Figure 10: Breaking Region Comparison For Different Hull Shapes.

28

displacement varies along with the hull shape in the examples shown. One would expect an increase in displacement to cause an increase in the amount of breaking independently of the hull shape, and the two effects are combined in these examples.

We next consider the effects of ship speed on the amount and distribution of wave breaking. Figure 11 shows an example of the frigate case where the triangular cross-hull taper and full taper along-hull were applied. Because we are making comparisons at different speeds, the sample spacing normalization described in Section 3.1 has been applied. Thus, the slower the ship speed, the smaller the sample spacing in the along-track direction and the larger the number of samples within the ship hull. In all examples a sample spacing of 1 meter in the cross-track direction was used. This figure shows that as the speed of the ship increases, the breaking area increases roughly in proportion to the ship speed. This dependence is in agreement with L-band SAR observations (Malinas, 1991) which show an increase in the NFDW radar cross section of about 0.3 dBsm per knot. This comparison tends to support our model, at least under assumption that the radar cross section is proportional to the breaking area.

The last hull characteristic to be considered is the hull outline at the water level. In all the previous examples, a frigate outline was used for illustration. Modifications to this outline are considered in this next example. Four different hull outlines are implemented in this current model. All have the bow of a frigate and a stern which is selectable. The options for the stern shape are (1) rectangular, (2) triangular, (3) elliptical, and (4) circular. Figure 12 illustrates these hull forms and the sample spacing used for the 18 knot case.

A comparison of the model output for three of these hulls is shown in Figure 13. The predicted dependence upon stern hull shape is very strong and perhaps counterintuitive, with the triangular hull shape producing more than 10 times as much breaking as the rectangular hull. This phenomenon results from the fact that the

29

Speed Comparison

Frigate Outline
Triangular Cross-hull Taper

25 knots

1400 m

Breaking Area: 930 m^2

18 knots

256 m

750 m

Breaking Area: 530 m^2

12 knots
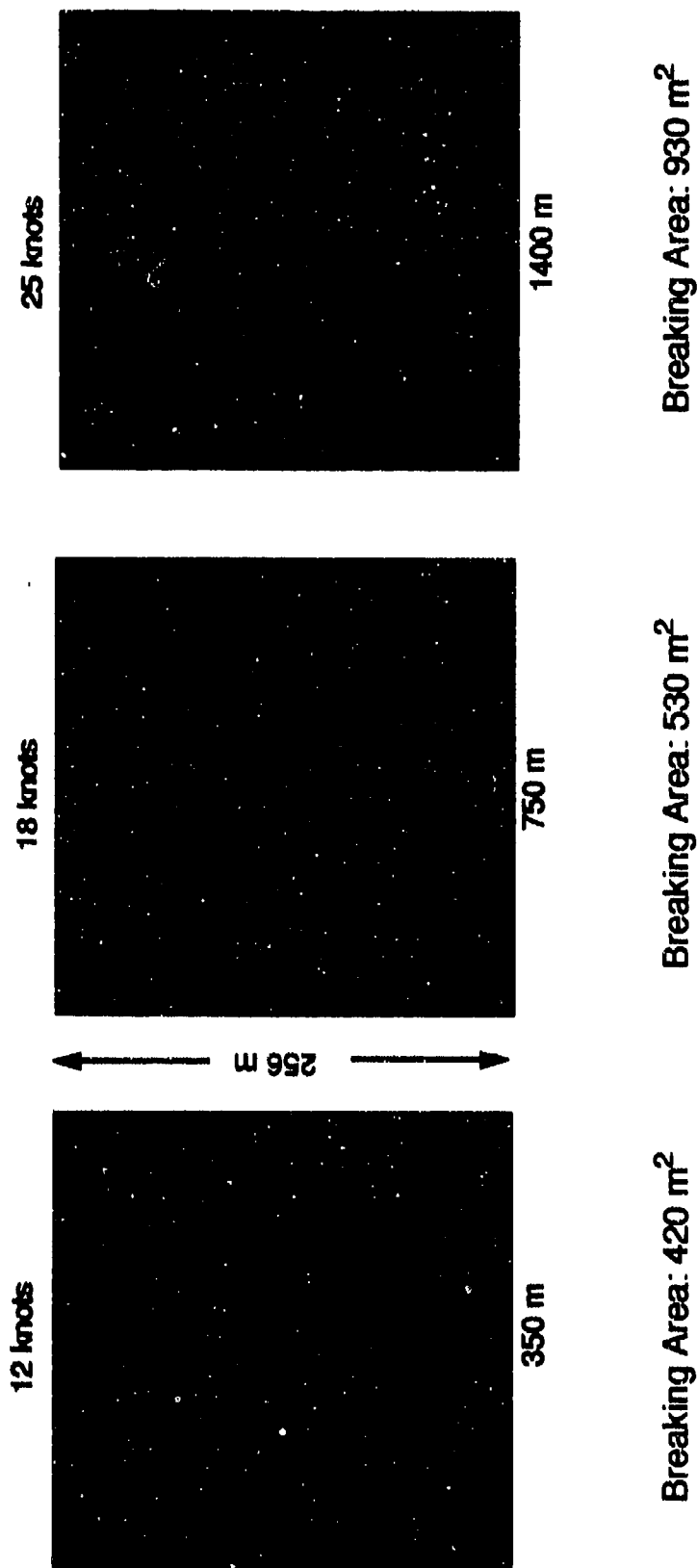
350 m

Breaking Area: 420 m^2

Figure 11: Breaking Region Comparison For Different Ship Speeds.
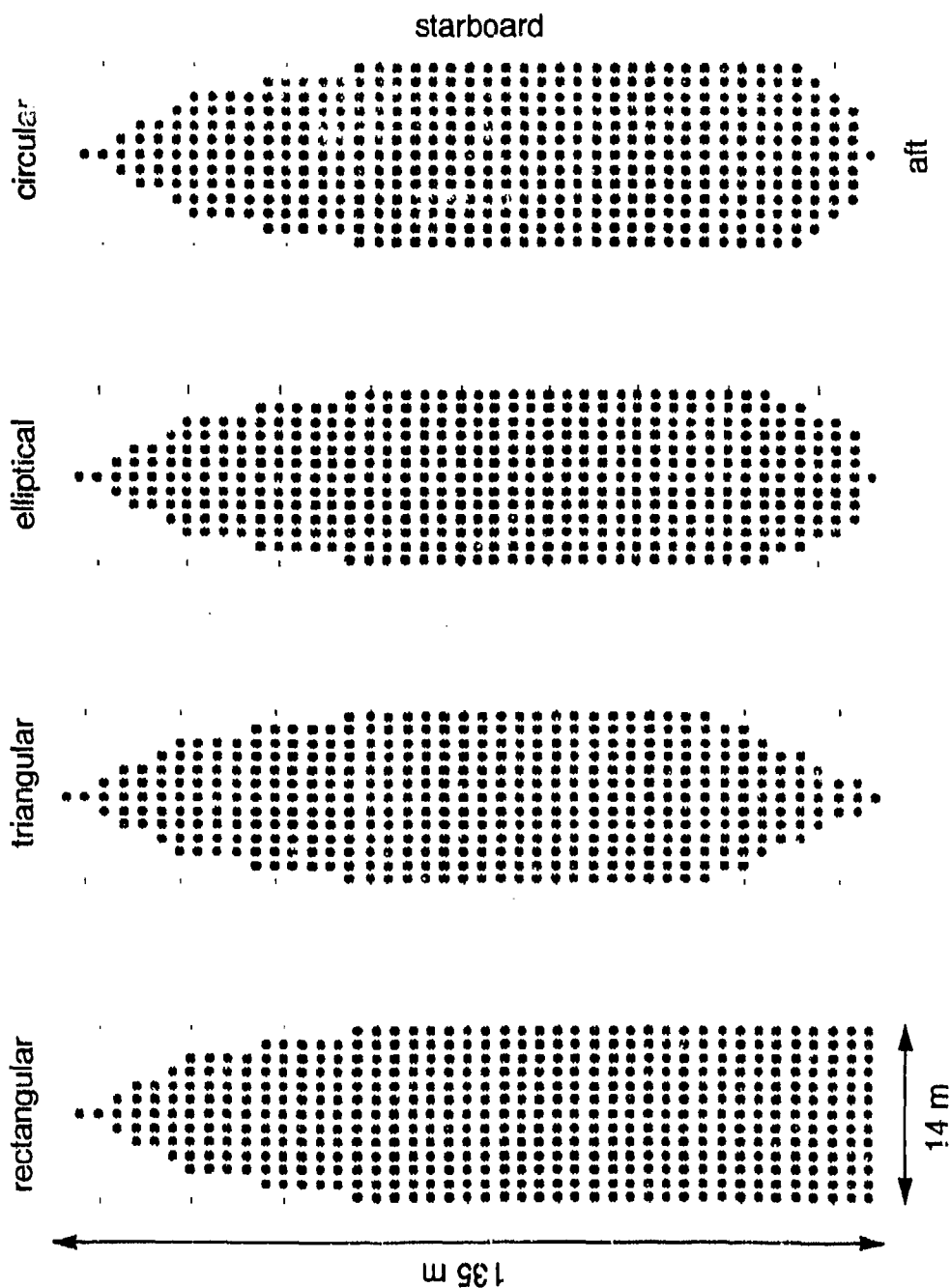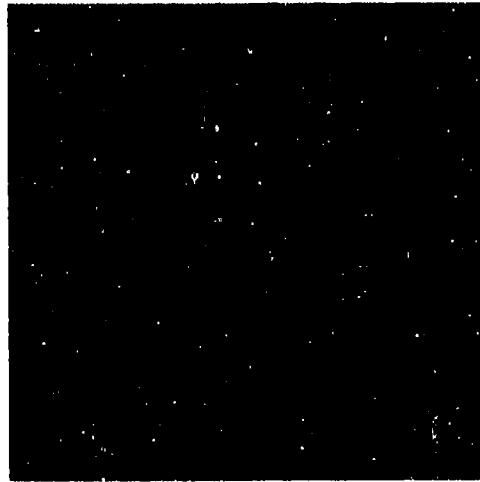
HULL SHAPE - Top View

Speed: 18 knots

Figure 12: Stern Hull Shapes Implemented Into Model.

Aft Outline Comparison

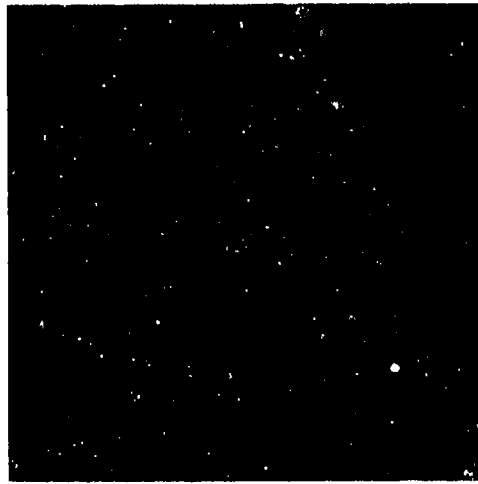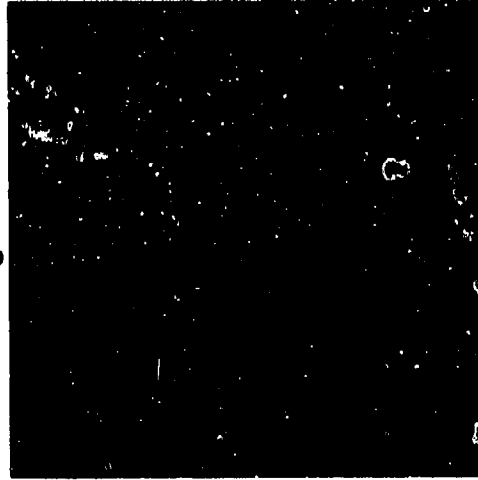## Triangular Cross-hull   18 Knot Ship Speed

Triangular Aft

Elliptical Aft

Rectangular Aft

Breaking Area: 350 m^2

Breaking Area: 1050 m^2

Breaking Area: 3750 m^2

Figure 13:   Breaking Region Comparison For Different Stern Hull Shapes.

spectrum of the pressure distribution for the rectangular stern is concentrated near the k_x-axis, and the spectral density in the cross-track direction falls off more rapidly for the rectangular than the non-rectangular shapes, as shown in Figure 14. The higher spectral density at large wavenumbers for the non-rectangular stern shapes is evident in the short wavelength of the breaking waves shown in Figure 13.

This figure also illustrates a general shortcoming of our model which arises from the neglect of energy dissipation due to wave breaking. Because there is no dissipation, waves which break near the hull continue to propagate and break at larger distances from the ship than is physically possible or realistic. That is, if we incorporated an energy dissipation due to breaking waves, most of the breaking would be confined to a region much closer to the ship than is indicated in Figure 13. This would also enforce a stronger wavenumber falloff, presumably as k^{-4}, in the wake spectrum.

Frequency Response Comparison

Surface Elevation Spectrum

Rectangular Aft
Triangular Cross-hull
U_s=18 knots

Surface Elevation Spectrum

Triangular Aft
Triangular Cross-hull
U_s=18 knots

Pressure Distribution

370 m

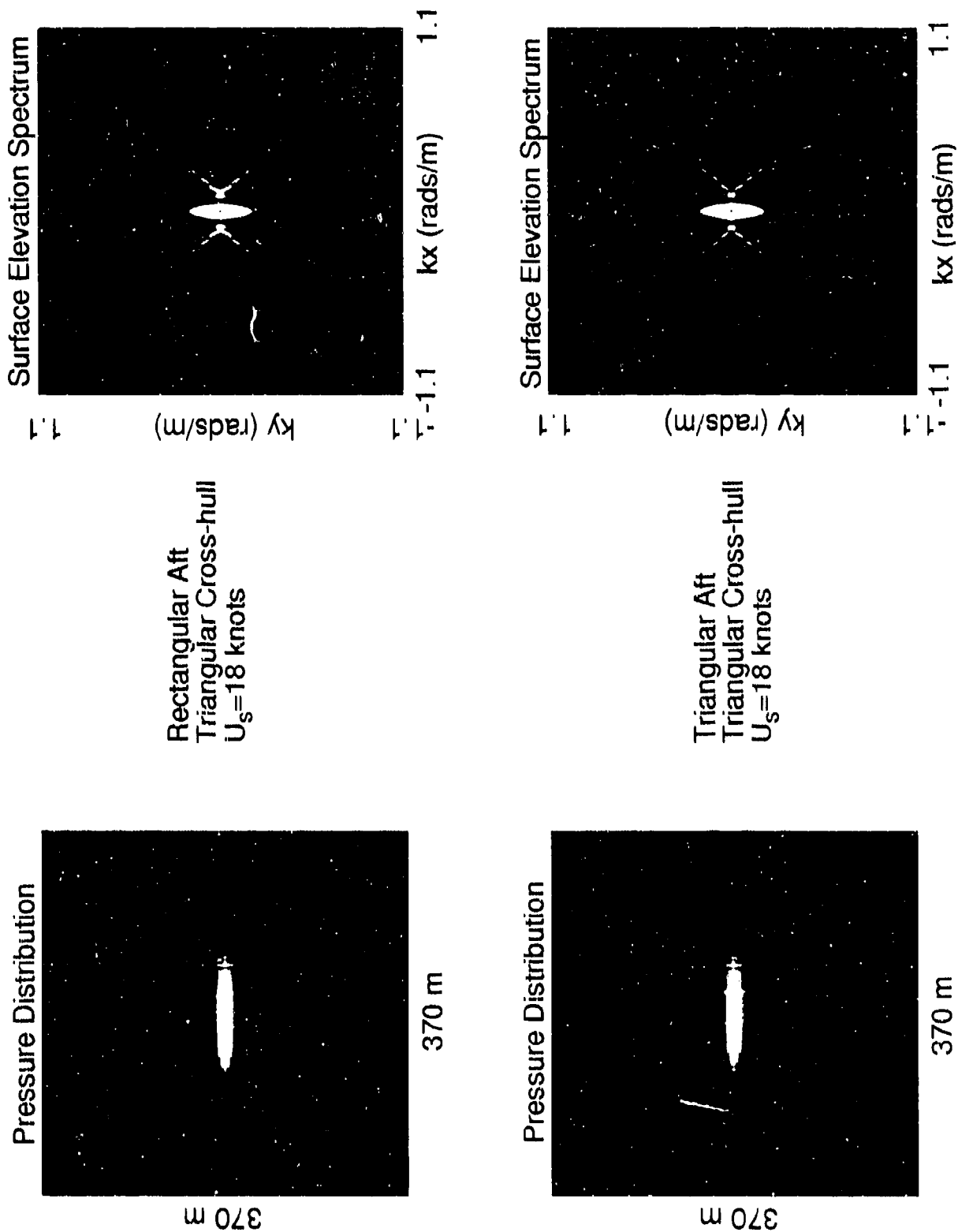## Pressure Distribution

370 m

Figure 14:   Surface Elevation Frequency Response Comparison For Different Stern Hull Shapes.

34

5.0 CONCLUSIONS AND RECOMMENDATIONS

A model has been developed for prediction of the near-field disturbed water region for a traveling ship. This model utilizes a Fourier transform solution for the Kelvin wake along with a numerical procedure for calculating the hull pressure distribution. The model appears to predict the breaking regions more or less correctly for ship hulls having a rectangular stern, but overpredicts the extent of the breaking regions for non-rectangular stern shapes. This limitation is apparently due to the fact that we have not included energy dissipation due to wave breaking.

We have used the outputs of our NFDW model to simulate the SAR image of this region and found encouraging agreement between the appearance of the simulated and actual SAR images. Furthermore, the dependence of the total radar cross section of the NFDW on ship speed is in agreement with observations.

Possible improvements to this model would include the incorporation of energy dissipation due to wave breaking, as mentioned above, and the development of a more detailed breaking wave reflectivity model based on laboratory measurements of the microstructure of breaking waves. Additional exercise of the model with more realistic hull shapes is also recommended.

REFERENCES

Ewing, J.A., M.S. Longuet-Higgins, and M.A. Srokosz, Measurements of the vertical acceleration in wind waves. *J. Phys. Oceanogr.*, *17*, 3-11, 1987.

Hasselmann, K., R.K. Raney, W.J. Plant, W. Alpers, R.A. Shuchman, D.R. Lyzenga, C.L. Rufenach, and M.J. Tucker, Theory of SAR ocean wave imaging: A MARSEN view, *J. Geophys. Res.*, *90*, 4659-4686, 1985.

Hoekstra, M., Macro Wake features of a Range of Ships, MARIN Technical Report No. 410461-1-PV, March, 1991, p.A1.8.

Jessup, A.T., W.K. Melville, and W.C. Keller, Breaking waves affecting microwave backscatter, 1. Detection and Verification, *J. Geophys. Res.*, *96*, 20547-20559, 1991.

Jessup, A.T., W.K. Melville, and W.C. Keller, Breaking waves affecting microwave backscatter, 2. Dependence on wind and wave conditions, *J. Geophys. Res.*, *96*, 20561-20569, 1991.

Kuhn, John C., An Assessment of the Inverse Kelvin Wake Computer Code Volumes I and II (U), SAIC Report DC# 92:01272, June 1992 (CLASSIFIED).

Lewis, B.L. and I.D. Olin, Experimental study and theoretical model of high-resolution radar backscatter from the sea, *Radio Sci.* *15*, 815-828, 1980.

Longuet-Higgins, M.S., Accelerations in steep gravity waves. *J. Phys. Oceanogr.*, *15*, 1570-1579, 1985.

Longuet-Higgins, M.S., On wave breaking and the equilibrium spectrum of wind-generated waves, *Proc. Roy. Soc. A.* *310*, 151-159, 1969.

Lyden, J.D., Ship Wake Experiment - Phase II, SAR Data Summary, ERIM Technical Memo RR-89-059, February, 1989.

Lyzenga, D.R., Numerical simulation of synthetic aperture radar image spectra for ocean waves, *IEEE Trans Geosci. Remote Sens.* *GE-24*, 863-872, 1986.

Malinas, N.P., Interim Data Analysis Report - DRAFT, ERIM Technical Report 242100-2-P, August, 1992.

⟩ERIM

REFERENCES (CONCLUDED)

Ochi, M.K. and C-H. Tsai, Prediction of occurrence of breaking waves in deep water, *J. Phys. Oceanogr.*, *13*, 2008-2019, 1983.

Phillips, O.M., The equilibrium range in the spectrum of wind generated waves. *J. Fluid Mech.*, *4*, 785-790, 1958.

Press, W.H. et.al., Numerical Recipes (Fortran), Cambridge University Press, New York, NY, pp. 38-39, 1989.

Snyder, R.L. and R.M. Kennedy, On the formation of whitecaps by a threshold mechanism. Part I: Basic Formalism. *J. Phys. Oceanogr.*, *13*, 1482-1492, 1983.

Kennedy, R.M. and R.L. Snyder, On the formation of whitecaps by a threshold mechanism. Part II: Monte Carlo experiments. *J. Phys. Oceanogr.*, *13*, 1493-1504, 1983.

Snyder, R.L., L. Smith and R.M. Kennedy, On the formation of whitecaps by a threshold mechanism. Part III: Field experiment and comparison with theory. *J. Phys. Oceanogr.*, *13*, 1505-1518, 1983.

Srokosz, M.A., On the probability of wave breaking in deep water. *J. Phys. Oceanogr.*, *16*, 382-385, 1986.

Walker, D.T., D. Lund, D. Lyzenga, and E. Ericson, Laboratory investigations of steadily breaking waves, presentation to URI advisory panel (manuscript in preparation), University of Michigan, November 1993.

Whitham, G.B., Linear and Nonlinear Waves, Wiley & Sons, New York, NY, 1974.